Korean J. Chem. Eng., 40(11), 2759-2770 (2023)
DOI: 10.1007/s11814-023-1499-7

pISSN: 0256-1115
eISSN: 1975-7220

Potential organic magnetic nanoparticles from peel extract of *Archidendron pauciflorum* for the effective removal of cationic and anionic dyes

Maya Rahmayanti*,†, Meilana Dharma Putra, Karmanto*, and Endaruji Sedyadi***

*Chemistry Department, Science and Technology Faculty, UIN Sunan Kalijaga Yogyakarta, Yogyakarta 55281, Indonesia
**Chemical Engineering Department, Faculty of Engineering Lambung Mangkurat University, Banjarbaru 70714, Indonesia
(*Received 19 March 2023 • Revised 1 May 2023 • Accepted 24 May 2023*)

Abstract–The adsorption of cationic (methylene blue, MB) and anionic (Congo red, CR) dyes using magnetic from *Archidendron pauciflorum* peel extract obtained via sonochemical synthesis (Fe_3O_4-AP) has been carried out. This study also compared the ability of Fe_3O_4-AP as an adsorbent for MB and CR through isotherm and kinetics studies. Fe_3O_4-AP was synthesized by the sonochemical method at a frequency of 800 kHz and characterized using FTIR, XRD, PSA, VSM and SEM-EDX. The XRD diffractogram showed Fe_3O_4-AP with high crystallinity with a crystal size of 17.05 nm, and the particle size distributed in three groups, 2.56, 862.23, and 4855.78 nm, respectively. Meanwhile, the Ms of Fe_3O_4-AP was 27.71 emu/g. The SEM-EDX showed disordered morphology with Fe, O and C elemental composition. The kinetics and isotherm of MB and CR dye adsorption on Fe_3O_4-AP followed Ho's kinetics model and Freundlich isotherm. The Freundlich isotherm model with adsorption capacities MB and CR on Fe_3O_4-AP was 16.02 and 10.24 mg/g, respectively.

Keywords: Magnetic Nanoparticles, *Archidendron pauciflorum* Peel Extract, Sonochemistry, Methylene Blue, Congo Red

INTRODUCTION

Synthetic dyes such as methylene blue and Congo red are the most widely used dyes in the textile industry [1,2]. Mostly, in the coloring process of the textile industry, it is only 45% of the dye that is attached to the cloth, while the rest is wasted in the washing process. Synthetic dyes in wastewater are unnaturally degraded and even have toxic properties; as a consequence, they must be processed before being discharged into the environment [1,3,4].

Many materials have been developed to treat dyes in wastewater. However, in recent years, materials with magnetic properties have received more attention in environmental remediation for being easier to regenerate and separate using an external magnetic field. Of the magnetic materials being developed, the magnetite compound (Fe_3O_4) is the most popular as it has a number of strong and more stable magnetic properties [5-11].

Plant extracts are some of the innovations of environmentally friendly magnetite synthesis. The specific content of organic compounds in plant extracts can act as the reducing agents and capping agents that control the growth process of material particles [12-14]. In addition, organic compounds can coat the magnetite materials' surface to prevent agglomeration [5,15,16]. The synthesis of magnetite nanomaterial using plant extracts has been widely developed using co-precipitation [17,18] and reverse co-precipitation [14,19]; however, the use of edible plant extracts will undermine food security.

Archidendron pauciflorum (Djengkol) plants are widely cultivated in tropical areas, especially in Southeast Asia [20]. The fruit's flesh is used as a food product in great demand. Along with the great market demand, the amount of peel waste also increases. Thus, the waste used as an added-value product becomes interesting to develop because it contributes to the environmental impact less and does not interfere with food security. The peel contains many compounds of tannins, saponins, alkaloids, glycosides, flavonoids, and steroids/triterpenoids [19] that can act as the reducing agents and capping agents in magnetite synthesis.

In this study, the developed magnetite using the peel of *Archidendron pauciflorum* was applied as an adsorbent for methylene blue and Congo red dyes. The sonochemical method was used in the synthesis process to obtain a smaller particle size. This method facilitates microscopic particle growth because the flow of ultrasonic waves can cause acoustic cavitation, which is the formation, growth, and bursting of liquid bubbles at very high temperatures and pressures (5,000 K, 20 MPa), followed by very high cooling rates (1010 K/S), resulting in extreme conditions. This extreme condition then leads to microscopic particle growth [21]. Magnetite synthesis using sonochemical method has been widely developed, but the synthesis of magnetite based on plant extracts using sonochemical methods has not been widely reported. In this research, the effectiveness of the developed magnetite using the peel of *Archidendron pauciflorum* obtained via sonochemical method for methylene blue and Congo red dyes adsorbent was studied through kinetics and adsorption isotherms.

EXPERIMENTAL

1. Materials

The plant waste used was *Archidendron pauciflorum* (locally called

†To whom correspondence should be addressed.
E-mail: maya.rahmayanti@uin-suka.ac.id

as djengkol) peel and the peel was further called as AP peel. The chemicals purchased from Merck Co were iron(III)chloride hexahydrate ($FeCl_3 \cdot 6H_2O$), iron(II)sulfate heptahydrate ($FeSO_4 \cdot 7H_2O$), sodium hydroxide (NaOH), hydrochloric acid (HCl), methylene blue and Congo red. The solvent used was water with twice distillation (aquabidest) from PT. Ikapharmindo.

2. Preparation of *Archidendron* Pauciflorum Peel Extract

The peel was dried in an oven at 60 °C for 2 hours, then cut into small pieces and mashed into powder. The organic compounds from peel powder were extracted using water as a solvent for 20 minutes at a temperature of 60 °C. The peel extract was then separated from the residue, and stored in the refrigerator. Before being used for synthesis, the extract must be left at a room temperature.

3. Sonochemical Synthesis of Fe_3O_4-AP

The magnetite produced from the peel of *Archidendron pauciflorum* using the sonochemical method was further named Fe_3O_4-AP. The sonicator used was the Leistungsfreq (generator type with a primary voltage of 230 V 50/60 Hz). A mixture of Fe^{3+} and Fe^{2+} precursors in a ratio of 2 : 1 was prepared by dissolving 2.164 g $FeCl_3 \cdot 6H_2O$ and 1.112 g $FeSO_4 \cdot 7H_2O$ with 100 mL aquabidest and then added to the NaOH 1 M solutions (1.6 g, 40 mL) by dropping them slowly. After the mixture of Fe^{3+} and Fe^{2+} precursors was dripped, the peel extract was poured. Stirring was continued for 60 minutes at a room temperature with an ultrasonic wave stream of 800 kHz. The precipitate and filtrate were separated by centrifugation using an external magnetic field.

4. Characterization of Fe_3O_4-AP

The Fe_3O_4-AP was characterized using FTIR, XRD, PSA, VSM and SEM-EDX. Functional group analysis used FTIR spectrophotometer (Shimadzu Prestige 21) in the transmission mode as the KBr method was used for all the powders. Crystallinity and crystal size of Fe_3O_4-AP, meanwhile, were determined using X-Ray diffraction (XRD-6000 Shimadzu) patterns recorded using a Bruker D2 phase diffractometer with Cu Kα (λ=0.1546 nm) radiation. Further, the particle size was determined by particle size analyzer (PSA) (Horiba SZ-100). The magnetization saturation of Fe_3O_4-AP was conducted using a vibrating sample magnetometer (VSM) and the analysis of morphology or surface structure and elemental content of Fe_3O_4-AP used scanning electron microscope-energy dispersive X-ray (SEM-EDX).

4-1. Determination of the Maximum Wavelength of MB and CR Dye Solutions

The MB and CR wavelengths were measured in the 400-700 nm wavelength range. Maximum wavelength information was used to construct the standard curves of MB and CR solutions. From the linear equations of the MB and CR standard curves, the concentrations of residual as well as the adsorbed MB and CR dyes could be then calculated.

5. Dye Adsorption Studies

MB and CR adsorption studies on Fe_3O_4-AP were performed by interacting MB and CR with Fe_3O_4-AP at various pH, adsorption time, and initial concentration of MB and CR.

5-1. pH Effect

A total of 25 mL of MB and CR dye solutions with a concentration of 15 ppm with a solution pH of 2, 4, 6, 8 and 10 interacted with 10 mg of Fe_3O_4-AP adsorbent for 60 minutes at room temperature. The adsorbent and filtrate of the mixture were separated by centrifugation using an external magnetic field. The amount of residual dye contained in the filtrate was analyzed using a UV-Vis spectrophotometer. The dye removal efficiency percentage (R%) was obtained from Eq. (1).

$$R\,(\%) = \left(\frac{C_0 - C_e}{C_0}\right) \times 100\% \quad (1)$$

6. Contact Time Effect and Kinetics Study

In the kinetic studies, the dye adsorption rate on the adsorbent surface and the mechanism between the dye and the adsorbent were evaluated. The adsorption kinetics of MB and CR on Fe_3O_4-AP was studied by interacting 10 mg of adsorbent Fe_3O_4-AP with 25 mL of MB dye and 15 ppm CR for 5-90 minutes. The interaction was carried out using the optimum dye pH and at room temperature. In this study, the three kinetic models used included Lagergren's pseudo-first-order, Ho's pseudo-second order, and Elovich's kinetic models.

7. Initial Dye Concentration Effect and Adsorption Isotherms Models

MB and CR adsorption isotherms on Fe_3O_4-AP were studied by interacting 10 mg of Fe_3O_4-AP adsorbent with MB and CR dyes of 5, 10, 15, 25 and 50 ppm, respectively, at room temperature with optimum dye pH and optimum reaction time. The adsorption capacity increased nonlinearly with increasing initial concentration [22].

RESULTS AND DISCUSSION

1. Characterization of Fe_3O_4-AP

The presence of functional groups in Fe_3O_4-AP can affect the adsorption ability of dyes [23]. The result of FTIR spectrophotometry was used to determine the type of functional group possessed by Fe_3O_4-AP. Based on the FTIR spectra as shown in Fig. 1, the functional groups of Fe_3O_4-AP could be derived from the func-

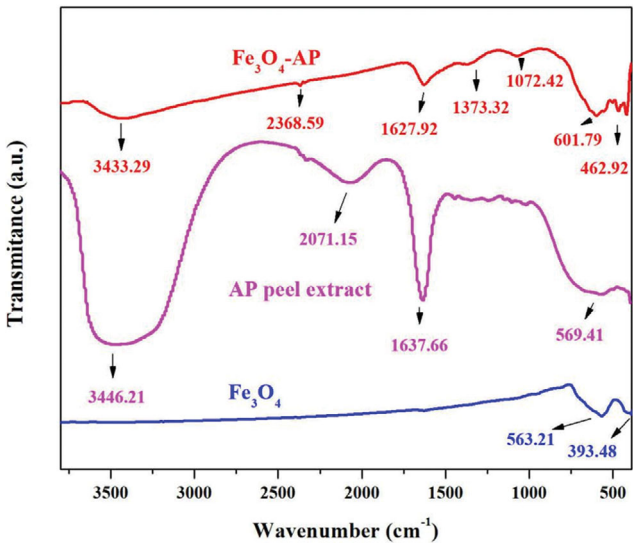

Fig. 1. FTIR spectra of pure Fe_3O_4, *Archidendron pauciflorum* peel extract and Fe_3O_4-AP.

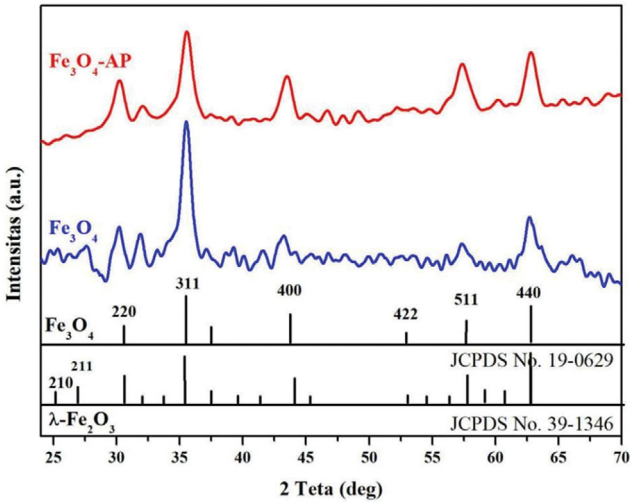

Fig. 2. XRD pattern of Fe_3O_4 and Fe_3O_4-AP.

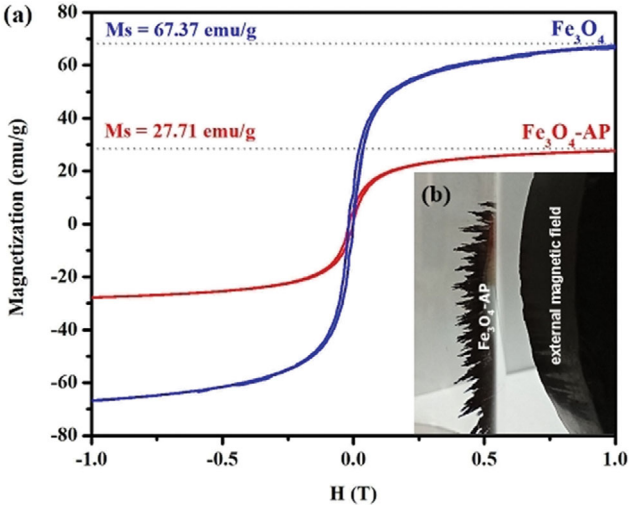

Fig. 3. (a) Magnetic properties of Fe_3O_4-AP (b) Magnetization curve at room temperature for Fe_3O_4-AP.

tional groups of pure Fe_3O_4 and AP peel extract. Absorption at wave numbers of 462.92 and 601.79 cm^{-1} in Fe_3O_4-AP indicated the presence of Fe_3O_4 in the form of Fe-O bonds. Compared to pure Fe_3O_4 spectra, an absorption shift was observed due to the interaction between the pure Fe_3O_4 surface and organic compounds in the AP peel extract. On the other hand, the absorption at the wave number of 462.92 cm^{-1} showed Fe-O bonds in octahedral units, while the absorption at 601.79 cm^{-1} showed Fe-O bonds in tetrahedral units [16,19,24,25].

The presence of functional groups of organic compounds derived from AP peel extract was indicated by the appearance of absorption at wave numbers 1,072.42, 1,373.32, 1,627.92, 2,368.59 and 3,433.29 cm^{-1}. These absorptions indicated the presence of C-O stretching vibrations, C=C aromatic compounds, -CH_2 stretching, and -OH group vibrations of carboxylic acids, alcohols, and phenols [26-28]. Though again there were absorption shifts due to new interactions compared to the AP peel extract, those indicated that Fe_3O_4-AP magnetic particles had been successfully synthesized from AP peel extract.

XRD characterization was carried out to determine the crystal structure of Fe_3O_4-AP as presented in Fig. 2. The Fe_3O_4-AP diffractogram showed the presence of intense peaks at the values of 2θ (Miller index) 30° (220), 35° (311), 43° (400), 53° (422), 57° (511), and 62° (440). These characteristic peaks belonged to Fe_3O_4 (JCPDS No. 19-0629). This confirmed that the magnetite (Fe_3O_4) formed did not mix with other iron oxides such as Fe_2O_3 (JCPDS No. 39-1346). This type of iron oxide led to stronger magnetic properties; it is thus more desirable as an adsorbent.

Fig. 3(a) shows the saturation magnetization (Ms) value of Fe_3O_4-AP. The presence of Fe_3O_4 in the AP peel extract contributed to a phenomenon of magnetization. The lower saturation magnetization observed for the AP peel extract during magnetite synthesis compared to the Fe_3O_4 was reasonable since the magnetization vectors for all domains in extensive materials such as AP peel extract containing various phenolic compounds could not be completely

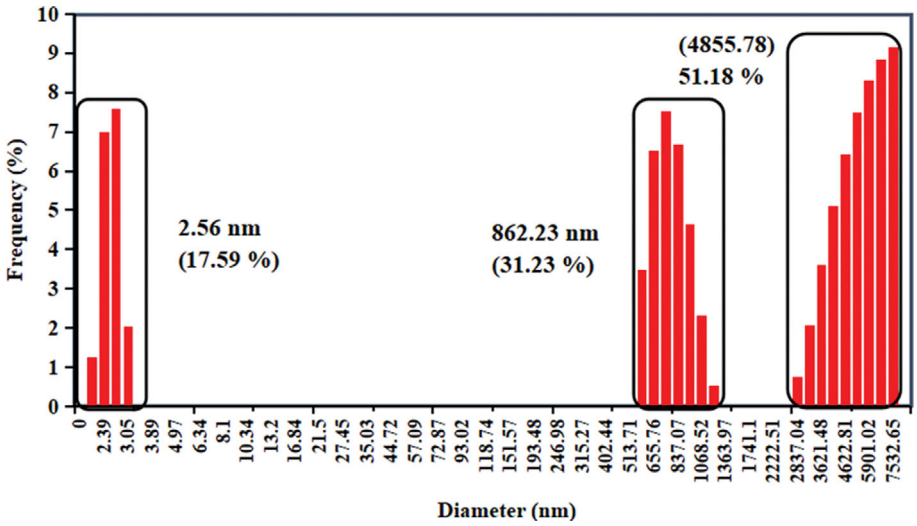

Fig. 4. Particle size distribution of Fe_3O_4-AP.

Table 1. Data of some plant-based magnetite particles

Extract source	Synthesis condition	Particle size (nm)	Morphology	Reference
Hevea brasiliensis Muell. Arg. peel	Conventional method Room temperature (27 °C), 1 h, $FeCl_3$ and $FeCl_2$	200 nm	-	[25]
Tea dregs	Conventional method pH 11, 60 min, 60 °C	2,670.37 nm	-	[29]
Archidendron pauciflorum	Conventional method, 60 min, 60 °C, $FeSO_4{\cdot}7H_2O$, $FeCl_3{\cdot}6H_2O$	318 and 294 nm	-	[19]
Archidendron pauciflorum	Sonochemical method, 60 min, 60 °C, $FeSO_4{\cdot}7H_2O$, $FeCl_3{\cdot}6H_2O$	2.56 nm, 862.23 nm, and 4,855.78 nm	Rough surface	This research

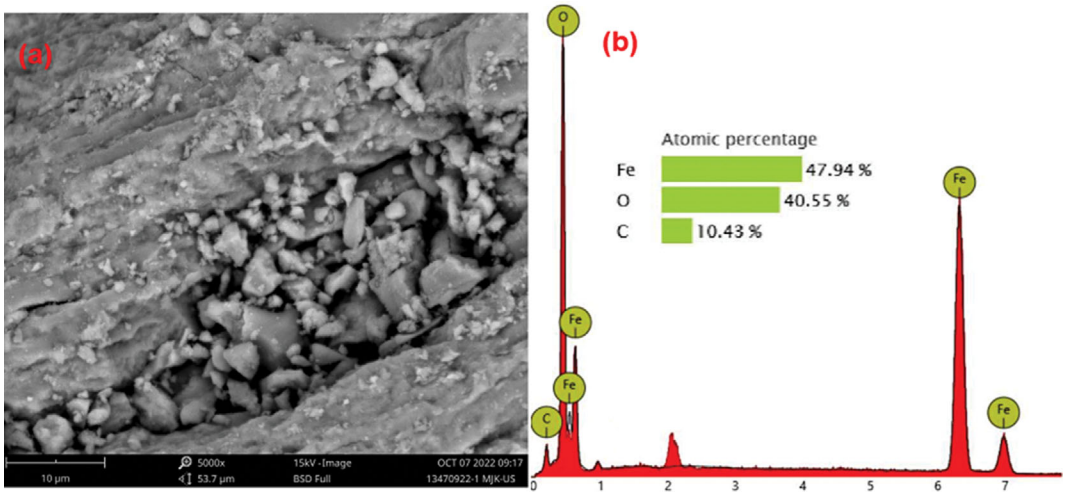

Fig. 5. (a) SEM images of Fe_3O_4-AP and (b) energy-dispersive X-ray fluorescence spectrometry spectra of Fe_3O_4-AP.

harmonized. Fig. 3(b) illustrates an image of Fe_3O_4-AP attracted to a magnetic field. The goal is to facilitate the separation process between the adsorbent and filtrate using an external magnetic field. The crystal size of Fe_3O_4-AP was determined using Debye-Scherrer's equation with full width at half maximum (FWHM=0.461) of the (311) reflection. The crystal size of Fe_3O_4 and Fe_3O_4-AP obtained in this study was 15.00 nm and 17.05 nm, respectively.

Fig. 4 presents the particle size distribution of Fe_3O_4-AP that was not uniform. There were three size groups with an average size of 2.56 nm, 862.23 nm, and 4,855.78 nm. Table 1 presents the comparison of particle size of the Fe_3O_4-AP with other magnetite particles. Compared to the previous studies, the sonochemical method succeeded in synthesizing Fe_3O_4-AP nanoparticles with smaller size, i.e., 2.56 nm.

Fig. 5(a) shows characterization results using SEM-EDX, and the image confirms the previous finding of using particle size analysis (PSA), as the magnetite particle size was here observed in the range of 1-5 µm. Fig. 5(b) shows the elemental content of Fe_3O_4-AP. The most significant percentage of elements was Fe, followed by O and C. This also reveals the role of Fe_3O_4 presence in the synthesis.

2. Synthesis Mechanism of Fe_3O_4-AP

Fe_3O_4-AP was synthesized using the reverse co-precipitation method at pH 12. The pH conditions of the synthesis greatly affected the purity of the Fe_3O_4-AP obtained. If the synthesis was conducted above pH 12, the iron oxide formed was magnetite (Fe_3O_4). Furthermore, if the synthesis was carried out below pH 8, other iron oxides such as hematite (Fe_2O_3) would be formed. According to the Pourbaix diagram of iron oxide, Fe_3O_4 is stable at pH 8 and Fe_2O_3 at pH 3 [19].

The original magnetite compounds had a pH_{PZC}=6-6.8 and the synthesis or modification method using organic compounds caused the pH_{PZC} magnetite to decrease into pH 3-4. The decrease in the pH_{PZC} value was caused by the protonation and deprotonation mechanism of the carboxylic acid group and the phenol hydroxy group with metal oxide nanoparticles [30-33].

In this study, Fe_3O_4-AP was synthesized at pH>pH_{PZC} Fe_3O_4. Under this condition, the surface of the magnetite was negatively charged. High solution pH (basic conditions) caused hydroxy ions (OH^-) to dominate in solution and then was able to extract H^+ from Fe-OH to produce negatively charged iron oxide species (Fe-O^-), as shown in Eq. (2) [34].

The negative surface of magnetite (Fe-O^-) will be able to interact with organic compounds such as tannins, flavonoids, and saponins through hydrogen bonds. Electrostatic interactions are difficult in this condition because these organic compounds' carboxylate and hydroxy groups have been protonated to -COO^- and -O^-

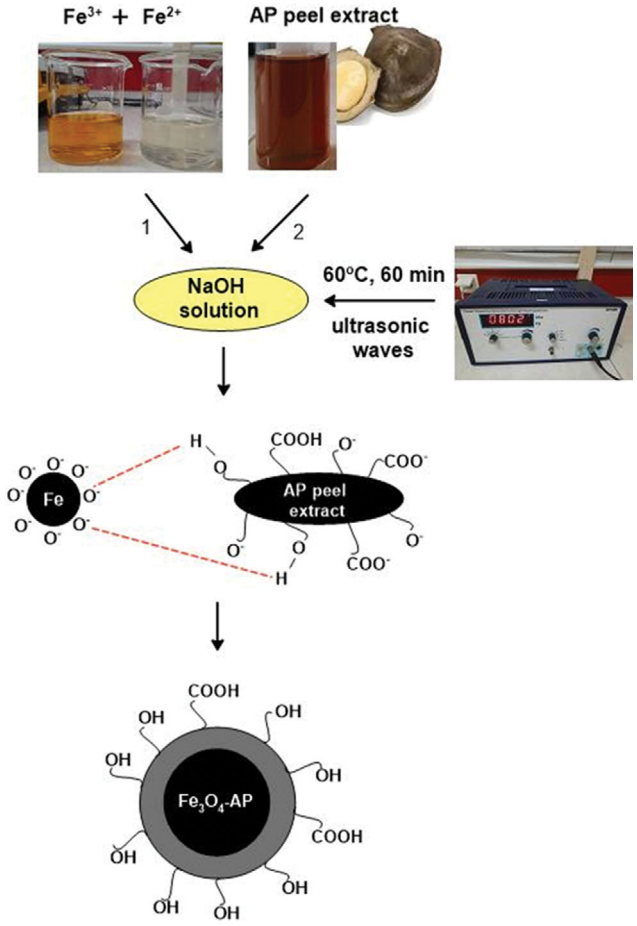

Fig. 6. Illustration of Fe_3O_4-AP synthesis.

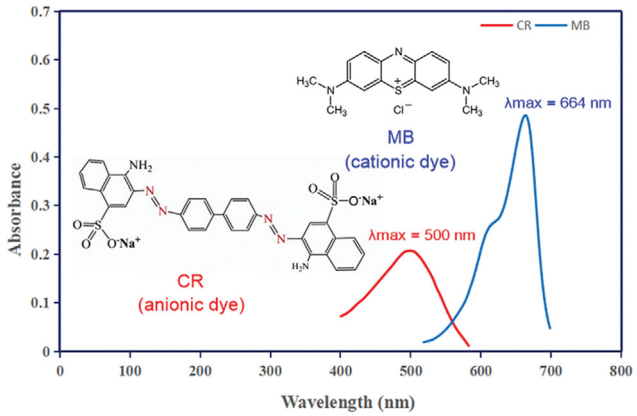

Fig. 7. Absorbance data of CR and MB dyes at various wavelengths.

[19]. Fig. 6 illustrates the synthesis mechanism of Fe_3O_4-AP as previously described.

3. Structure and Maximum Wavelength of the Dye

Fig. 7 presents the graphs of the wavelengths of CR and MB dyes. The determination of the peak wavelength of dye was required to evaluate the concentration of dye adsorbed on Fe_3O_4-AP. The peak wavelength of CR dyes was 500 nm, while the maximum wavelength of MB was 664 nm.

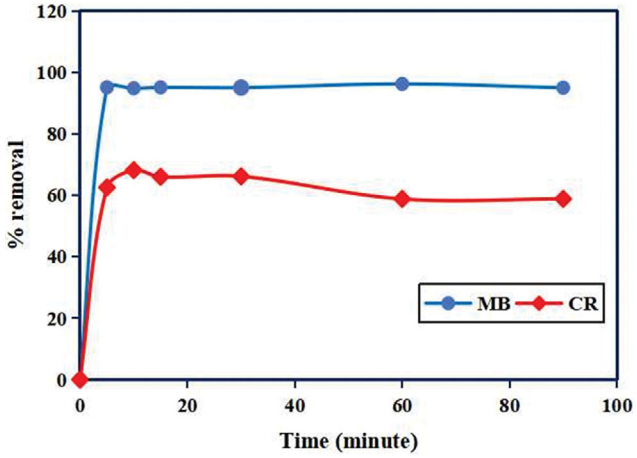

Fig. 8. Kinetic profile of adsorption of MB and CR (pH 4, [MB or CR]=15 ppm and room temperature) using Fe_3O_4-AP.

4. Adsorption Study of Cationic and Anionic Dyes on Fe_3O_4-AP

4-1. Kinetic Profile of the MB and CR Adsorption on Fe_3O_4-AP

The kinetic profile of MB and CR adsorption using Fe_3O_4-AP had a similar pattern as shown in Fig. 8. Adsorption occurred rapidly in the early minutes until the fifth minute equilibrium was reached. After reaching equilibrium, there was no significant increase or decrease in MB or CR removal. The surface condition of Fe_3O_4-AP at the beginning of the interaction was still unsaturated, thus allowing the abundant active groups in Fe_3O_4-AP to interact very quickly with MB and CR. After reaching equilibrium, the surface of Fe_3O_4-AP became saturated; hence, the adsorption of MB and CR no longer increased. It was also observed that the ability of Fe_3O_4-AP to adsorb MB was better than CR due to differences in the chemical structure of MB and CR related to the previous pH discussion. Further explanation regarding these findings would be further confirmed through studies of kinetics and isotherms adsorption.

4-2. Effect of Dye Initial Concentration on the Adsorption Ability of Fe_3O_4-AP

Fig. 9 presents the relationship between the initial concentrations of MB and CR and the adsorption ability of Fe_3O_4-AP. The adsorption of MB and CR on Fe_3O_4-AP increased until the initial concentration of MB and CR reached 15 ppm. However, the adsorption ability of Fe_3O_4-AP decreased, at which the initial dye concentration was higher than 15 ppm. The decrease in % removal at the initial dye concentration ≥15 ppm was because, at high concentrations, the dyes would compete with each other to interact with the Fe_3O_4-AP adsorbent. The optimum % removal of MB and CR was 97 and 91%, respectively.

4-3. Effect of Dye pH on Fe_3O_4-AP Adsorption Ability

Fig. 10 presents the results of the pH optimization for dye removal by Fe_3O_4-AP. The Fe_3O_4-AP adsorbent had a pH_{PZC}=3. The surface conditions of Fe_3O_4-AP at pH above and below pH_{PZC} were different. Various previous studies have reported that a solution's initial pH conditions greatly affected a magnetic particle's adsorption ability [35-37]. It is reported for pH above pH_{PZC}, the surface of Fe_3O_4-AP was negatively charged due to the deprotonation of

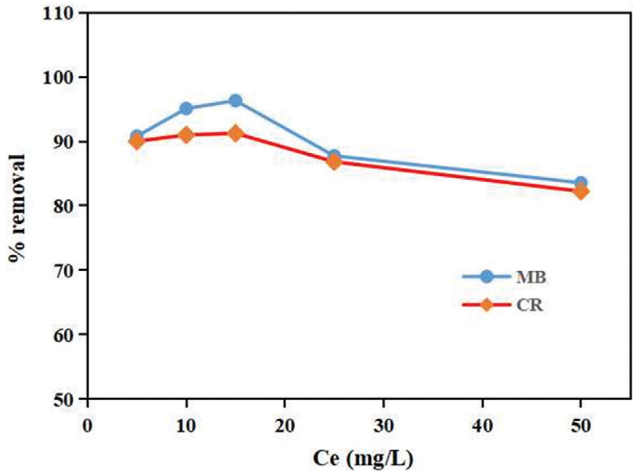

Fig. 9. Adsorption of MB and CR at various dye initial concentrations (pH 4, t=30 min, room temperature).

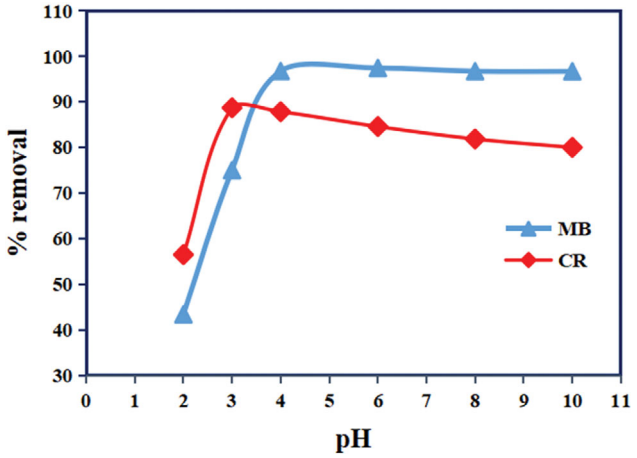

Fig. 10. pH optimization for dye removal by Fe_3O_4-AP.

-OH and -COOH groups into $-O^-$ and $-COO^-$ groups. For pH under pH_{PZC}, the surface of Fe_3O_4-AP was positively charged due to the protonation of the -OH and -COOH groups into $-OH_2^+$ and $-COOH_2^+$ groups [18,19]. Thus, the difference in the surface charge of the adsorbent affected the ability of Fe_3O_4-AP to adsorb dyes as here caused by pH. As observed in Fig. 8, MB dye adsorption using Fe_3O_4-AP led to a great performance of % removal at pH>3, and the ability of adsorption decreased at pH<3. It was plausible because MB is a cationic dye with S^+ or N^+ groups, thus easily interacting through electrostatic connections with $-O^-$ and $-COO^-$ groups on the surface of Fe_3O_4-AP which were negatively charged at pH>3; hence, MB adsorption on Fe_3O_4-AP could reach 96-97%. Meanwhile, at pH≤3, % MB removal was only around 43-75%. At this pH condition, the surface of Fe_3O_4-AP was positively charged; thus, electrostatic interactions between S^+ or N^+ of MB with $-OH_2^+$ and $-COOH_2^+$ Fe_3O_4-AP groups were increasingly difficult to occur.

The adsorption of CR on Fe_3O_4-AP was found better than the adsorption of MB on Fe_3O_4-AP at a pH below pHPZC Fe_3O_4-AP. CR is an anionic dye with SO_3^- groups, thus making it easier to interact with the positive Fe_3O_4-AP surface (pH<3) through electrostatic interactions between the SO_3^- groups of CR dyes with $-OH_2^+$ and $-COOH_2^+$ from the Fe_3O_4-AP adsorbent. Above pH 3, the ability of Fe_3O_4-AP to adsorb CR decreased because the -OH and -COOH groups of the Fe_3O_4-AP adsorbent had been deprotonated into $-O^-$ and $-COO^-$ groups; hence, electrostatic interactions were increasingly challenging to occur. However, the percentage of the removal was still above 80%. From this phenomenon, it was suspected that the electrostatic interaction mechanism was not the only mechanism between MB and CR with Fe_3O_4-AP.

Other possible interaction models were hydrogen bonding, π-π interactions and hydrophobic interactions [38-40,50]. Hydrogen bonds occur between the hydrogen atoms of the $-OH_2^+$ and $-COOH_2^+$ Fe_3O_4-AP groups with the nitrogen atoms of the $-N(CH_3)_2$ group of MB or between the oxygen atoms of the $-O^-$ and $-COO^-$ groups and the hydrogen atoms of the $-CH_2$ and $-NH_2$ groups of CR. Meanwhile, π-π interactions occur between π bonds in Fe_3O_4-AP due to the delocalization of the charge distribution of the conjugated aromatic ring with bonds in the aromatic ring of MB or CR dyes.

On the other hand, hydrophobic interaction is an interesting proposed mechanism because of the interaction between a hydrophobic molecule and dye molecules in an aqueous solution. When Fe_3O_4-AP (hydrophobic) meets aqueous solution molecules (MB and CR), hydrogen bonds will be broken between aqueous solution molecules to provide a space for Fe_3O_4-AP. However, aqueous solution molecules do not react with Fe_3O_4-AP. This process is considered as an endothermic reaction because heat will enter the system when a bond is broken. Furthermore, the aqueous solution molecules are distorted due to the presence of Fe_3O_4-AP molecules that form new hydrogen bonds between the aqueous solution molecules and further yield a clathrate cage around the Fe_3O_4-AP molecules. Fig. 11 illustrates the interaction mechanism between Fe_3O_4-AP with cationic and anionic dyes. The illustration is also strengthened by the post-adsorption Fe_3O_4-AP characterization results using an FTIR spectrophotometer as presented in Fig. 12. Since there was no new absorption peak in the post-adsorption of MB and CR on Fe_3O_4-AP spectra, the interaction between MB and CR with Fe_3O_4-AP occurred through physical interactions.

4-4. Kinetics Studies

In this study, the three kinetic models used included Lagergren's pseudo-first-order, Ho's pseudo-second order, and Elovich's kinetic models. Lagergren's equation of pseudo-first order is presented in Eq. (3). The adsorption capacity of MB and CR dyes on Fe_3O_4-AP at time t (minutes) and equilibrium are expressed by q_t and q_e (mg/g), and the pseudo-first-order reaction rate constant is expressed by k_1 (min^{-1}). If a graph of $\ln(q_e - q_t)$ versus t were made, it would produce a straight line with slope and intercept. The value of k_1 was obtained from the slope, and the value of q_e was obtained from the intercept.

$$\ln(q_e - q_t) = \ln q_e - k_1 t \quad (3)$$

Ho's pseudo-second-order equation is expressed in Eq. (4). Like Lagergren's pseudo-first-order equation, the adsorption capacities of MB and CR dyes on Fe_3O_4-AP at time t (minutes) and equilibrium are expressed by q_t and q_e (mg/g), respectively. For Ho's pseudo-second-order, the constant is expressed by k_2 (g/mg·min). The advantage of this model is that it could calculate the initial dye

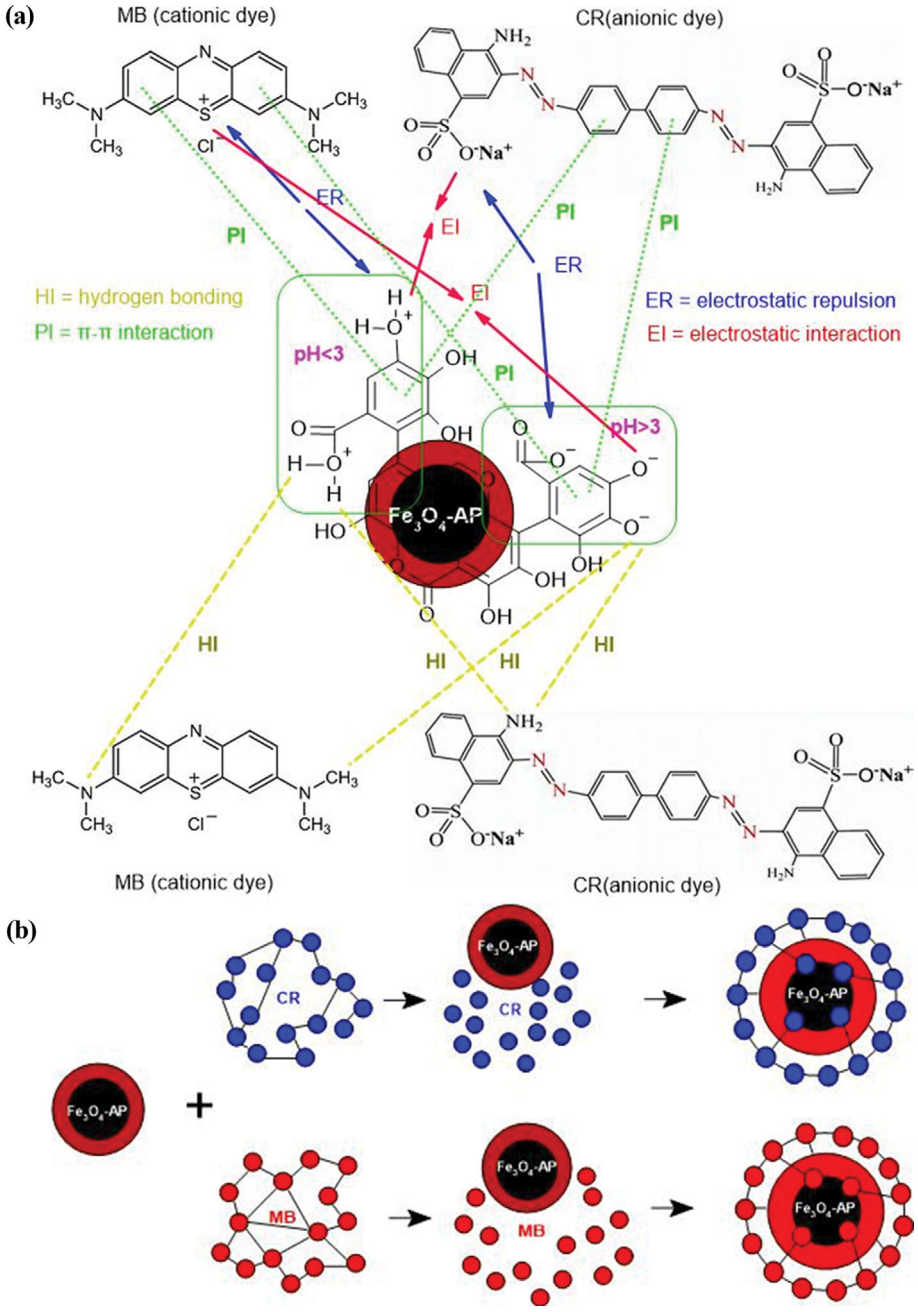

Fig. 11. Illustration of the interaction mechanism between Fe_3O_4-AP with cationic and anionic dyes.

adsorption rate on Fe_3O_4-AP (mg/g·min) with the formula presented in Eq. (5). The values of q_e and k_2 were determined from the slope and intercept of the graph of t/q_t versus t.

$$\frac{t}{q_t}=\frac{1}{k_2q_e^2}+\frac{1}{q_e}t \tag{4}$$

$$h=k_2q_e^2 \tag{5}$$

Elovich's kinetic model is expressed in Eq. (5). This kinetic model is suitable for the adsorption of gases and wastewater pollutants [41]. The desorption constant associated with the surface area and chemisorption activation energy is expressed by β (g/mg), and the initial adsorption rate is expressed by α (mg/g min). By making a graph of lnt versus q_t, the α and β values are determined from the slope and intercept.

$$q_t=\left(\frac{1}{\beta}\right)\ln(\alpha\beta)+\left(\frac{1}{\beta}\right)\ln(t) \tag{6}$$

Fig. 13 and Table 2 presents the graphs of the MB and CR adsorption kinetic models on Fe_3O_4-AP. Kinetic studies showed that the adsorption of MB and CR on Fe_3O_4-AP followed the pseudo-second-order Ho's kinetic model with R^2 values of 1 and 0.9965, respectively, and did not match with the Lagergren pseudo-first-order kinetic model with R^2 of 0.1959 and 0.098, respectively. These indi-

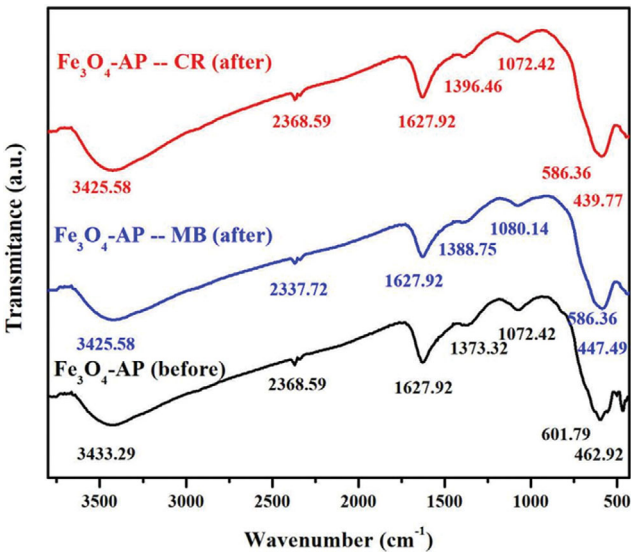

Fig. 12. FTIR spectra of Fe_3O_4-AP before and after adsorption.

cated that the adsorption of MB and CR involved more than two active sites belonging to the Fe_3O_4-AP surface [42]. In addition, the adsorption of MB and CR on Fe_3O_4-AP was determined by the adsorbent, adsorbate and water solvent used. The kinetics study of MB and CR adsorption on Fe_3O_4-AP using the Elovich model resulted in R^2 values of 0.6504 and 0.5851, respectively, meaning that the adsorption of MB and CR on Fe_3O_4-AP also did not follow this kinetic model. Elovich's kinetic model assumes that dye adsorption on Fe_3O_4-AP occurs at a local site, interactions between dye ions are possible, and dye concentration is considered to be constant [41]. The results of this kinetic study reinforced the presumption of the previously described interaction mechanism.

Table 2. Kinetic parameters of MB and CR dyes

Kinetic models	Parameters	Dyes	
		MB	CR
Lagergren's pseudo-first-order	**R^2**	**0.1959**	**0.098**
	q_e (mg/g)	0.960	2.330
	k (min^{-1})	0.001	0.0166
Ho's pseudo-second-order	**R^2**	**1.0000**	**0.9965**
	q_e (mg/g)	1,666.67	1,250.00
	h (mg/g·min)	14,285.71	1,666.67
	k (g/mg·min)	0.00514	0.00107
Elovich	**R^2**	**0.6504**	**0.5851**
	α (mg/g·min)	0.804	0.773
	β (g/mg)	0.003	0.004

4-5. Isotherm Studies

The adsorption isotherm was studied to determine the relationship between the initial concentrations of MB and CR dyes and the adsorption capacity of Fe_3O_4-AP when the dye was initially distributed in equilibrium between the solid and liquid phases. In this

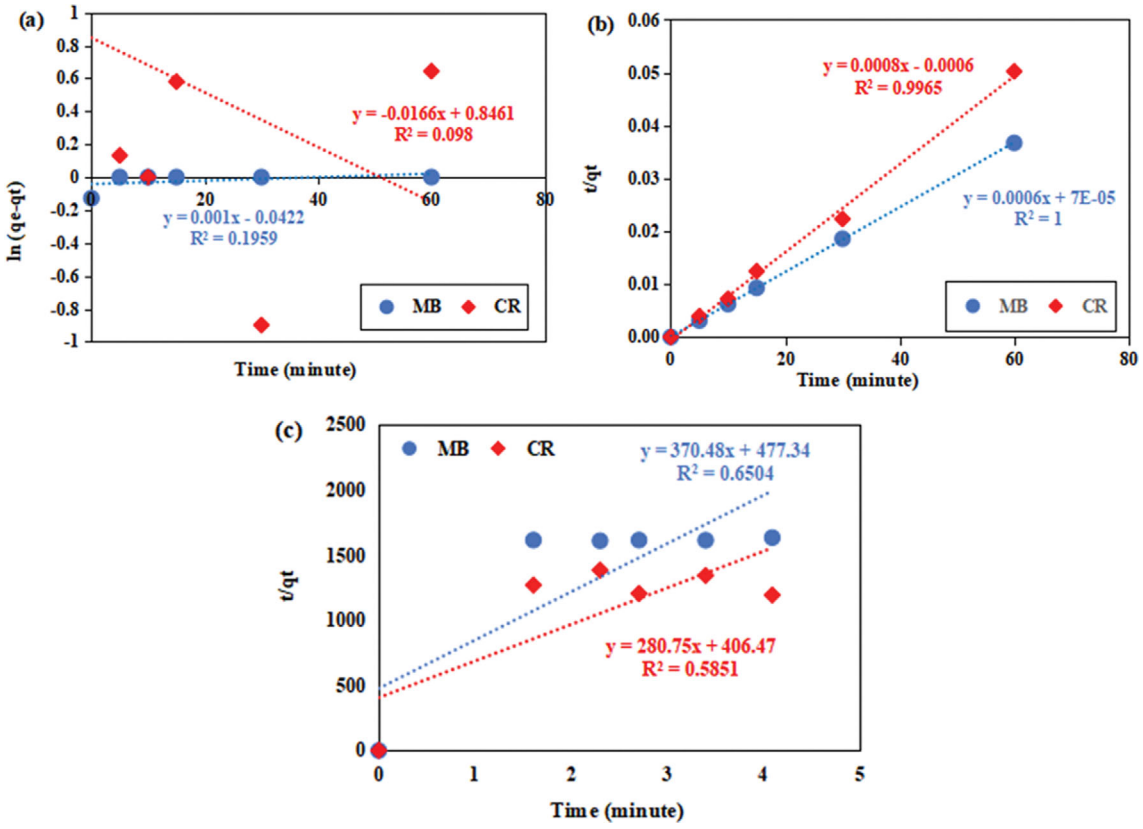

Fig. 13. (a). Lagergren's pseudo first-order (b) Ho's pseudo second (c) Elovich's kinetic models of MB and CR adsorption onto Fe_3O_4-AP.

study, three adsorption isotherm models were used: Langmuir, Freundlich and Temkin isotherm.

Langmuir isotherm model is expressed in Eq. (7) and the concentration of free dye ions in solution at equilibrium is expressed as C_e (mg/L). The amount of dye adsorbed at equilibrium and the maximum single-layer adsorption capacity is expressed by q_e and q_{max} (mg/g), respectively. Meanwhile, K_L is the Langmuir constant associated with the adsorption energy, describing the affinity of the dye for Fe_3O_4-AP (L/mg). By plotting C_e/q_e versus C_e, the q_{max} and K_L are calculated from the slope and intercept, respectively.

$$\frac{C_e}{q_e}=\frac{1}{K_L q_{max}}+\left(\frac{1}{q_{max}}\right)C_e \tag{7}$$

The Freundlich isotherm equation is expressed in Eq. (8) and the equilibrium adsorption capacity is expressed by q_e (mg/g) [43]. C_e refers to the concentration of free dye ions in solution at equilibrium (mg/L). The Freundlich constant associated with adsorption capacity is expressed as K_F (mg/g). By making a graph of $\log q_e$ versus $\log C_e$, the values of n and K_F are evaluated with the slope and intercept. 1/n refers to a heterogeneity factor that indicates the intensity of dye adsorption on Fe_3O_4-AP. The value of n indicates the preferred adsorption process and is in the $0.1<1/n<1$ [44,45].

$$\log q_e=\log K_F+\left(\frac{1}{n}\right)\log C_e \tag{8}$$

The Temkin isotherm model is expressed in Eq. (9). Similar to the kinetic model of Langmuir and Freundlich, q_e (mg/g) and C_e (mg/L) refer to the equilibrium adsorption capacity and the concentration of free dye ions in solution at equilibrium, respectively. B corresponds to the heat of adsorption, and k_T is the binding constant of the Temkin isotherm at equilibrium and is associated with the maximum binding energy. The relationship between B and the adsorption potential of the adsorbent is expressed in Eq. (10), where R is the universal gas constant (8.314 J/kmol); T is the temperature (K), and $1/b_T$ (mol/J) is the adsorption potential of the adsorbent.

$$q_e=B\ln k_T+B\ln C_e \tag{9}$$

$$B=\frac{RT}{b_T} \tag{10}$$

The Temkin isotherm model was studied to determine the adsorbent-adsorbate interaction. This model assumes that the heat adsorption of all molecules in the layer decreased linearly with surface coverage. In addition, the adsorption energy, when the adsorption site was filled, decreased linearly. Likewise, the binding energy distribution was uniform up to the maximum value. By making a graph of q_e versus $\ln C_e$, the values of B and K_T were determined by slope and intercept values.

Based on Fig. 14 and Table 3, Freundlich and Temkin adsorption isotherms well fitted the data for MB and CR adsorption isotherms on Fe_3O_4-AP with values of $R^2>0.9$. However, the Freundlich

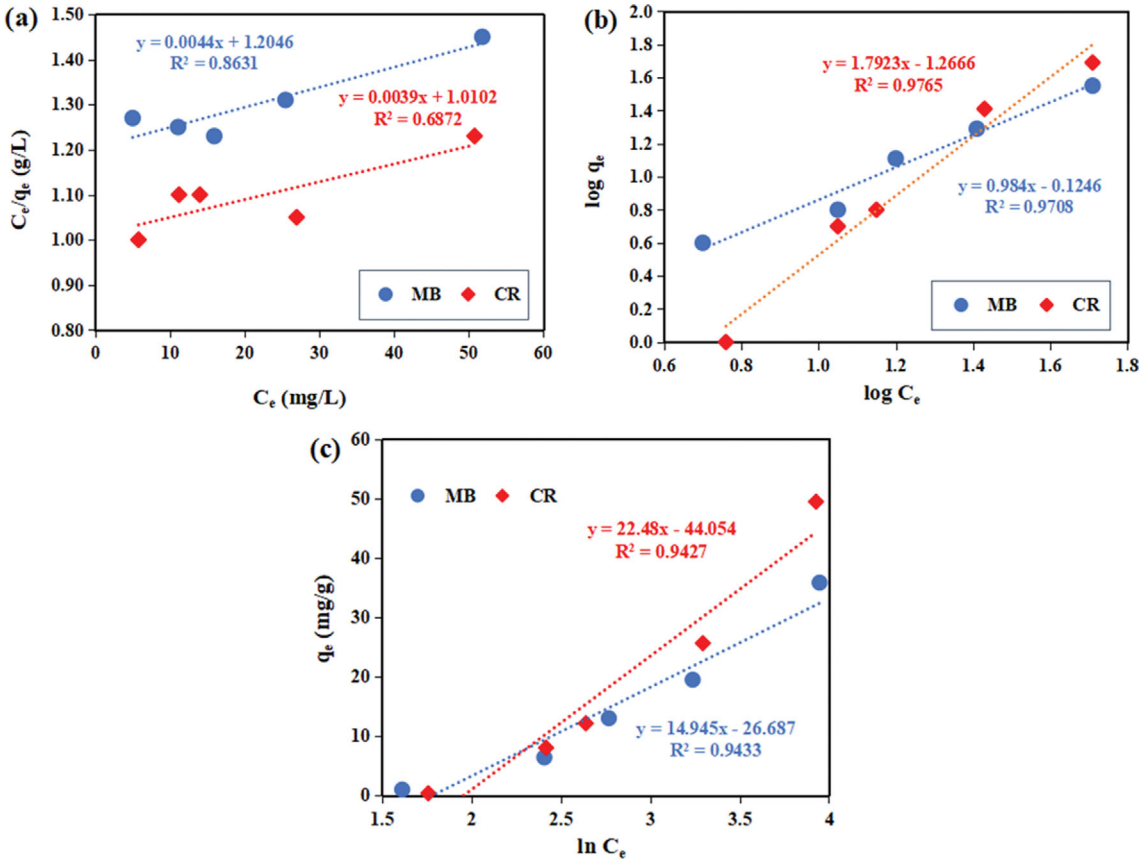

Fig. 14. (a). Langmuir, (b) Freundlich, and (c) Temkin isotherm models of MB and CR adsorption onto Fe_3O_4-AP.

Table 3. Isotherm parameters of MB and CR dyes

Isotherm models	Parameters	Dyes	
		MB	CR
Langmuir	q_{max} (mg g^{-1})	227.27	256.41
	K_L (L mg^{-1})	0.0037	0.0039
	E_{ads} (kJ mg^{-1})	−14,044.86	−13,906.29
	R^2	**0.8631**	**0.6872**
Freundlich	K_F (mg g^{-1})	16.02	10.24
	n	1.016	0.558
	R^2	**0.9708**	**0.9765**
Temkin	B	14.95	22.48
	k_T (L mg^{-1})	0.17	0.14
	$1/b_T$	0.0060	0.0091
	R^2	**0.9443**	**0.9427**

adsorption isotherm was found to better perform with the higher values of the R^2. Freundlich isotherm model showed that various active sites played an important role in the adsorption process and had different adsorption energies but with the same entropy [43]. This finding aligned with the adsorption kinetics studies that followed Ho's second-order kinetic model. Based on Eq. (7), it was also observed that the value of 1/n for MB adsorption (0.98) was smaller than 1 compared to the value for CR adsorption (1.80), indicating that the intensity of MB dye adsorption on Fe_3O_4-AP was more favorable.

In addition, the value of 1/n below 1 indicates that the adsorption operation was physical instead of chemical (for the value of 1/n higher than 1) [44]. This also strengthened the alleged MB adsorption mechanism on Fe_3O_4-AP as described previously through physical adsorption. On the other hand, the preferred CR adsorption on Fe_3O_4-AP was chemical, while the FTIR characterization of the post-adsorption adsorbent did not show the formation of new adsorption due to chemical interactions. It became the reason that the KF value of MB adsorption on Fe_3O_4-AP was higher than the K_F value of CR adsorption on Fe_3O_4-AP.

On the other hand, for the Temkin isotherm model (R^2>0.9), the heat of adsorption of all molecules in the aqueous solution of MB and CR dyes decreased linearly with the range. The adsorbent-adsorbate interaction and adsorption were characterized by the regular allocation of binding energy until it reached the maximum binding energy [46]. Based on the $1/b_T$ value, which showed the potential of the adsorbent, the adsorbent Fe_3O_4-AP had a better CR adsorption potential than MB. However, the binding constant value of the Temkin isotherm was obtained at equilibrium and was associated with a lower maximum binding energy (k_T) for CR adsorption compared to MB.

5. Performance of Fe_3O_4-AP as MB and CR Adsorbent

Table 4 presents the previously reported adsorption studies of various adsorbents for MB and CR removal compared with the results of this study. Compared with the results of other studies related to the adsorption of MB and CR dyes, Fe_3O_4-AP had an

Table 4. MB and CR adsorption studies

Adsorbate	Adsorbent	% Removal	Kinetic model	Fitted isotherm model	References
MB	Porous activated Starbons® derived from starch	82.6%	Pseudo-second-order and Elovich	Freundlich isotherm	[47]
MB	Orange and lemon peels-derived activated carbon (OLPAC)	98.0%	Pseudo-second-order model	Langmuir isotherms	[26]
MB	Activated carbon of Coriandrum sativum	95.0%	Pseudo-second-order kinetic	Temkin	[27]
MB	Magnetite nanoparticles using Archidendron pauciflorum peel extract (conventional)	91.7%	Pseudo-second-order kinetic	Freundlich isotherm	[19]
MB	Magnetite using Archidendron pauciflorum peel extract (sonochemical)	97%	Pseudo-second-order kinetic	Freundlich isotherm	This research
CR	MgAl-layered double hydroxide (MgAl-LDH)	14.8-100%	Pseudo-second-order kinetic	Langmuir isotherms	[40]
CR	Magnetic nanocellulose base polymeric ionic liquid	91-100%	-	Langmuir isotherms	[48]
CR	Magnetite-nanoparticle-decorated NiFe LDH (MNPs@NiFe LDH)	96%	Pseudo-second-order kinetic	Langmuir isotherms	[49]
CR	Magnetite using Archidendron pauciflorum peel extract (sonochemical)	91%	Pseudo-second-order kinetic	Freundlich isotherm	This research

excellent adsorption ability even though it was synthesized using plant waste extracts. Another advantage is that adsorbents were found to be more environmentally friendly, whereas extraction solvents used was water with lower production costs. Thus, Fe_3O_4-AP has the potential to be developed as an adsorbent for MB and CR dyes.

CONCLUSIONS

Fe_3O_4-AP synthesized using the sonochemical method has great potential as an adsorbent for methylene blue and Congo red dyes in simulated wastewater. Fe_3O_4-AP synthesized using sonochemistry has high crystallinity, crystal size, and smaller particles compared to conventional methods, and other plant extracts studied previously. Also, the Fe_3O_4-AP adsorbent has superparamagnetic properties with a saturation magnetization value of 27.71 emu/g. The adsorption of MB and CR on Fe_3O_4-AP follows a pseudo-second-order Ho kinetic model with qe values of 1,666.67 and 1,250.00 mg/g, respectively, and k values of 0.00514 and 0.00107 g/mg.min, respectively. The MB and CR adsorption isotherms on Fe_3O_4-AP follow the Freundlich isotherm model with KF values of 16.02 and 10.24 mg/g, respectively. Fe_3O_4-AP was found to be capable of absorbing MB dye better than CR dye.

ACKNOWLEDGEMENTS

The authors would like to thank the Institute for Research and Community Service UIN Sunan Kalijaga Yogyakarta for the 2022 research grant for a research cluster of higher education collaborations. The authors also thank Mr. Wijayanto as laboratory assistant from the UIN Sunan Kalijaga Integrated Laboratory who has accompanied the research team in completing this research. In addition, the authors also thank Dr. Khurul Wardati as dean of the Faculty of Science and Technology, UIN Sunan Kalijaga for administrative support.

REFERENCES

1. F. M. Valadi, A. Ekramipooya and M. R. Gholami, *J. Mol. Liq.*, **318**, 114051 (2020).
2. Q. Wei, Y. Zhang, K. Zhang, J. I. Mwasiagi, X. Zhao, C. W. K. Chow and R. Tang, *Korean J. Chem. Eng.*, **39**, 1850 (2022).
3. Y. Zheng, X. Sun, X. Liu, X. Xia, L. Xiao, C. Cao, Q. Qian and Q. Chen, *Ind. Crops Prod.*, **171**, 113930 (2021).
4. T. K. N. Tran, V. T. Le, T. H. Nguyen, V. D. Doan, Y. Vasseghian and H. S. Le, *Korean J. Chem. Eng.*, **40**, 1650 (2023).
5. H. S. Devi, M. A. Boda, M. A. Shah, S. Parveen and A. H. Wani, *Green Process. Synth.*, **8**, 38 (2019).
6. M. Mabrouk, R. M. A. El-Wahab, H. H. Beherei, M. M. Selim and D. Das, *Int. J. Pharm.*, **587**, 119658 (2020).
7. E. Guo, G. Chen, D. Yu, Y. Qiu, S. Li and Y. Yu, *J. Environ. Chem. Eng.*, **10**, 108618 (2022).
8. N. S. El-Gendy and H. N. Nassar, *Sci. Total Environ.*, **774**, 145610 (2021).
9. K. Lakshmi and R. Rangasamy, *J. Mol. Struct.*, **1224**, 129081 (2021).
10. M. Rahmayanti, I. Nurhikmah and F. Larasati, *Mol. Biol. (Mosc.)*, **16**, 68 (2021).
11. W. Liu, H. Bai, W. Gao, Z. Chen, Z. Liu, Z. Chen and J. Chen, *Korean J. Chem. Eng.*, **39**, 2792 (2022).
12. A. Sebastian, A. Nangia and M. N. V. Prasad, *J. Hazard. Mater.*, **371**, 261 (2019).
13. S. Fakhari, M. Jamzad and H. Kabiri Fard, *Green Chem. Lett. Rev.*, **12**, 19 (2019).
14. F. Azadi, A. Karimi-Jashni and M. M. Zerafat, *Ecotoxicol. Environ. Saf.*, **165**, 467 (2018).
15. C. V. Khedkar, N. D. Khupse, B. R. Thombare, P. R. Dusane, G. Lole, R. S. Devan, A. S. Deshpande and S. I. Patil, *Chem. Phys. Lett.*, **742**, 137131 (2020).
16. A. Sebastian, A. Nangia and M. N. V. Prasad, *J. Cleaner Prod.*, **174**, 355 (2018).
17. L. Hiremath, N. K. Sura and P. Sukanya, *Mater. Today Proc.*, **5**, 21030 (2018).
18. H. Luo, S. Zhang, X. Li, X. Liu, Q. Xu, J. Liu and Z. Wang, *J. Taiwan Inst. Chem. Eng.*, **72**, 163 (2017).
19. M. Rahmayanti, A. Nurul Syakina, I. Fatimah and T. Sulistyaningsih, *Chem. Phys. Lett.*, **803**, 139834 (2022).
20. S. Charungchitrak, A. Petsom, P. Sangvanich and A. Karnchanatat, *Food Chem.*, **126**, 1025 (2011).
21. M. Rahmayanti, S. J. Santosa and S. Sutarno, *Adv. Mater. Res.*, **1101**, 286 (2015).
22. H. Zheng, D. Liu, Y. Zheng, S. Liang and Z. Liu, *J. Hazard. Mater.*, **167**, 141 (2009).
23. J. Wang and X. Guo, *J. Hazard. Mater.*, **390**, 122156 (2020).
24. Y. P. Yew, K. Shameli, M. Miyake, N. Kuwano, N. B. Bt Ahmad Khairudin, S. E. Bt Mohamad and K. X. Lee, *Nanoscale Res. Lett.*, **11**, 276 (2016).
25. H. Rasoulzadeh, A. Mohseni-Bandpei, M. Hosseini and M. Safari, *Int. J. Biol. Macromol.*, **133**, 712 (2019).
26. D. Ramutshatsha-Makhwedzha, A. Mavhungu, M. L. Moropeng and R. Mbaya, *Heliyon*, **8**, e09930 (2022).
27. C. C. de Souza, L. Z. M. de Souza, M. Yılmaz, M. A. de Oliveira, A. C. da Silva Bezerra, E. F. da Silva, M. R. Dumont and A. R. T. Machado, *Clean. Mater.*, **3**, 100052 (2022).
28. P. C. Nnaji, V. C. Anadebe, I. G. Ezemagu and O. D. Onukwuli, *Arab. J. Chem.*, **15**, 103629 (2022).
29. M. Rahmayanti, A. Yahdiyani and I. Q. Afifah, *Commun. Sci. Technol.*, **7**, 119 (2022).
30. L. Ouma and A. Ofomaja, *RSC Adv.*, **10**, 2812 (2020).
31. M. Rahmayanti, S. J. Santosa and S. Sutarno, *Indones. J. Chem.*, **16**, 329 (2016).
32. S. V. Bhosale, S. R. Suryawanshi, S. V. Bhoraskar, M. A. More, D. S. Joag and V. L. Mathe, *Mater. Res. Express*, **2**, 095001 (2015).
33. S. Nigam, K. C. Barick and D. Bahadur, *J. Magn. Magn. Mater.*, **323**, 237 (2011).
34. M. Masuku, L. Ouma and A. Pholosi, *Environ. Nanotechnol. Monit. Manag.*, **15**, 100429 (2021).
35. T. Babacan, D. Doğan, Ü. Erdem and A. Ü. Metin, *Mater. Chem. Phys.*, **284**, 126032 (2022).
36. M. Shamsipur and A. Ghavidast, *J. Mol. Struct.*, **1263**, 133130 (2022).
37. B. S. Damasceno, A. F. V. da Silva and A. C. V. de Araújo, *J. Environ. Chem. Eng.*, **8**, 103994 (2020).
38. R. Foroutan, R. Mohammadi and B. Ramavandi, *Environ. Sci. Pol-*

lut. Res., **26**, 19523 (2019).
39. C. González-Galán, A. Luna-Triguero, J. M. Vicent-Luna, A. P. Zaderenko, A. Sławek, R. Sánchez-de-Armas and S. Calero, *Chem. Eng. J.*, **398**, 125678 (2020).
40. M. A. Farghali, A. M. Selim, H. F. Khater, N. Bagato, W. Alharbi, K. H. Alharbi and I. Taha Radwan, *Arab. J. Chem.*, **15**, 104171 (2022).
41. L. Largitte and R. Pasquier, *Chem. Eng. Res. Des.*, **109**, 495 (2016).
42. M. Benjelloun, Y. Miyah, G. Akdemir Evrendilek, F. Zerrouq and S. Lairini, *Arab. J. Chem.*, **14**, 103031 (2021).
43. H. Freundlich, *Z. Phys. Chem.*, **57U**, 385 (1907).
44. J. Bensalah, A. Habsaoui, O. Dagdag, A. Lebkiri, I. Ismi, E. H. Rifi, I. Warad and A. Zarrouk, *Chem. Data Collect.*, **35**, 100756 (2021).
45. J. Xie, T. Yamaguchi and J.-M. Oh, *J. Solid State Chem.*, **293**, 121758 (2021).
46. M. Temkin and V. Pyzhev, *Acta Physiochim. URSS*, **12**, 327 (1940).
47. H. Li, V. L. Budarin, J. H. Clark, M. North and X. Wu, *J. Hazard. Mater.*, **436**, 129174 (2022).
48. M. H. Beyki, M. Bayat and F. Shemirani, *Bioresour. Technol.*, **218**, 326 (2016).
49. T. Taher, R. Putra, N. Rahayu Palapa and A. Lesbani, *Chem. Phys. Lett.*, **777**, 138712 (2021).
50. A. N. Syakina and M. Rahmayanti, *Chem. Data Collect.*, **44**, 101003 (2023).